Decoupling Control of MSM Rotor with Heavy Self-weight and Great Moment of Inertia Based on Internal Model Control

Biao Xiang[1][*]and Waion Wong[1]

1, Department of Mechanical Engineering, The Hong Kong Polytechnic University, Kowloon,

Hong Kong SAR, China

*Corresponding author: thomas.biao@gmail.com

Abstract—The control performance of magnetically suspended motor (MSM) with heavy self-weight and great moment of inertia is affected by parameter uncertainty and external disturbances, and the coupling effect in radial tilting of MSM becomes serious with the increase of rotational speed and moment of inertia, and then the robustness would be reduced. Therefore, an internal model control (IMC) model is proposed to adjust the robustness of MSM. Based on the IMC model, a decoupling IMC model is designed for MSM on four degrees of freedom. Simulation and experiment are conducted to verify that the IMC model improves the robust stability of MSM, and the decoupling IMC model effectively realizes the decoupling control of MSM on four degrees of freedom.

Index Terms: magnetically suspended motor; coupling effect; internal model control; decoupling control; robust stability

1. Introduction

The magnetically suspended rotational machine has been widely applied in high-speed motors (Li et al., 2020), centrifugal compressors (Han et al., 2016)，pumps (Asama et al., 2014; Masuzawa et al., 2003; Wang et al., 2019) and robot system (Cole and Fakkaew, 2018) because of its advantages on controllability (Xiang and Tang, 2015; Barbaraci, 2016), zero-friction (Xiang and on Wong, 2019; Barbaraci et al., 2013) and lubrication-free (Cui and Cui, 2017). The PID control is a common method (Parada et al., 2017; Wei and Söffker, 2016; Tang et al., 2017; Ahrens et al., 1996) to realize the displacement control of MSM rotor. Other control schemes were also used to displacement control of MSM rotor to improve control performances on response speed, tracking precision and robustness. For example, the feed-forward control was used to reduce the vibration response of a magnetically suspended motor (MSM) (Zheng and Feng, 2016). In addition, the robust control (Noshadi et al., 2017; Rubio, 2018; Pesch et al., 2015), the sliding mode control (Zad et al., 2018; Rubio et al., 2019)

and the fuzzy control (Couzon and Der Hagopian, 2007; Haiping et al., 2010) were used to the displacement control of MSM rotor. However, those MSM rotors in above-mentioned literatures are 'normal' size, so the self-weight did not cause serious influence on the displacement control.

For the MSM rotor with heavy self-weight, the displacement stiffness and the current stiffness easily deviate from nominal values, so this kind of MSM rotor is more sensitive to external disturbances and parameter uncertainty than 'small' MSM rotors (Guo et al., 2016). There are coupling terms in radial rotations of MSM rotor, and they become significant with the increase of rotational speed.

Moreover, the internal model control (IMC) has characteristics on virtually affecting robustness through parameter design, so the stability of control system is guaranteed, and the structural model identification of control plant is not needed. Therefore, the robustness of control plant was tuned by adjusting the filter parameter (Garcia and Morari, 1982; Rivera et al., 1986). An IMC model with cross-coupling integrator was applied to a permanent magnet synchronous machine (PMSM) (Zad et al., 2018). The analysis results showed that the IMC model had lower parameter sensitivity, and an oscillation was avoided by applying a decoupling IMC (DIMC). A speed regulation strategy based on an IMC model and fuzzy adaptive law was designed to mitigate the sensitivity to input saturation and to improve speed tracking precision. It automatically tuned control parameters of rotational speed (Li and Gu, 2012). A control strategy combining an inverse system and an IMC model was proposed to mitigate the gyroscopic effect in a magnetically suspended control moment gyro (Fang and Ren, 2010), and it was proved that the IMC model is useful on suppressing gyroscopic terms of MSM rotor. Based on the inverse system theory and an IMC model, a decoupling control scheme was designed for an active magnetic bearing (AMB) to suppress unmodeled dynamics (Sun et al., 2017).

Therefore, the IMC and DIMC models are potential to improve the robustness of MSM rotor with heavy self-weight and great moment of inertia. The robust stability of MSM rotor could be regulated by the IMC model, and the coupling effect could also be mitigated. In this article, an IMC model is designed for an MSM rotor with heavy self-weight and great moment of inertia. The DIMC model could realize the decentralized control of MSM rotor on four DOFs, so the robust stability of MSM rotor at high rotational speed could be improved.

This article is organized as follows. In section 2, structure and dynamic models of MSM

rotor are introduced. The IMC and DIMC models are designed in section 3. The simulations are conducted in section 4. The experiments are conducted to compare performances of two control models in section 5. Finally, conclusions are summarized in section 0.

2. Structure and Modeling of MSM Rotor

2.1. Modelling of MSM Rotor
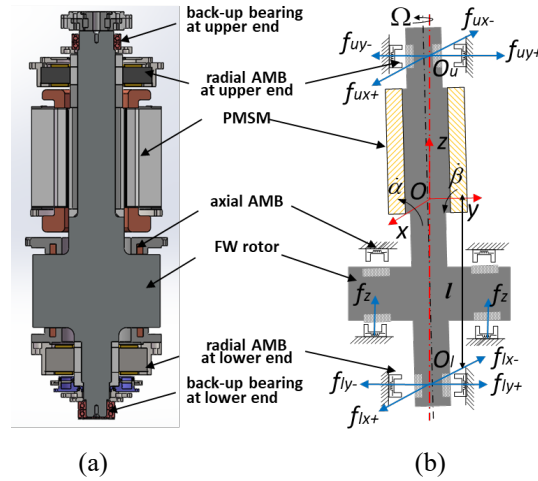

<div align="center">(a)   (b)</div>

Fig. 1. (a) prototype of MSM rotor, (b) force analysis of simplified model.

The structure of an MSM rotor is depicted in Fig. 1(a); and it consists of a rotor system and a suspension system. The rotor system contains a flywheel (FW) rotor with 150Kg and a PMSM. The suspension system has a magnetic suspension system and a backup ball bearing system. The axial AMBs at lower and upper end of FW rotor stably suspend it at the axial equilibrium point. The radial AMBs at lower and upper end control radial translation and tilting of MSM rotor. As a protective component, the backup ball bearings hold the MSM rotor upright when the magnetic suspension system fails to work.

The force analysis of MSM rotor is plotted in Fig. 1(b). The rotation about the axial axis is controlled by the PMSM, and the motions in other five DOFs are controlled by axial and radial AMBs. Considering the lower radial displacement sensor is symmetric to upper displacement sensor in axial direction, for radial translation and radial tilting of MSM rotor, the equations of motion are

<div align="center">3</div>

$$\begin{cases} m\ddot{d}_x = f_{ux+} - f_{ux-} + f_{lx+} - f_{lx-} = f_{ux} + f_{lx} \\ m\ddot{d}_y = f_{uy+} - f_{uy-} + f_{ly+} - f_{ly-} = f_{uy} + f_{ly} \\ J_x\ddot{\alpha} = f_{uy} \times l - f_{ly} \times l + J_z\Omega\dot{\beta} \\ J_y\ddot{\beta} = f_{ux} \times l - f_{lx} \times l - J_z\Omega\dot{\alpha} \end{cases} \quad (1)$$

where $J_x=J_y$ is equatorial moment of inertial, and J_z is polar moment of inertial. d_x and d_y are radial displacements along x-axis and y-axis, respectively. l is the suspension span of radial AMB. α and β are tilting angles about radial axes, respectively. Ω is rotational speed about z-axis.

The MSM rotor works at the balanced state when resultant forces and torques acting on it equal to zero. If not, it is at a nonequilibrium state. For example, the MSM rotor tilts an angle α about x-axis in Fig. 1(b). Since the suspension span of upper radial AMB is same as that at lower end, radial displacements and tilting angles are

$$\begin{cases} d_x = \left(d_{ux} + d_{lx}\right)/2; \quad d_y = \left(d_{uy} + d_{ly}\right)/2 \\ \alpha = \left(d_{uy} - d_{ly}\right)/2l; \quad \beta = \left(d_{ux} - d_{lx}\right)/2l \end{cases} \quad (2)$$

The equations of motion are rewritten into

$$\begin{cases} m\left(\dfrac{\ddot{d}_{ux} + \ddot{d}_{lx}}{2}\right) = f_{ux} + f_{lx} \\ m\left(\dfrac{\ddot{d}_{uy} + \ddot{d}_{ly}}{2}\right) = f_{uy} + f_{ly} \\ J_x\dfrac{\left(\ddot{d}_{uy} - \ddot{d}_{ly}\right)}{2l} = f_{uy} \cdot l - f_{ly} \cdot l + J_z\Omega\dfrac{\left(\dot{d}_{ux} - \dot{d}_{lx}\right)}{2l} \\ J_y\dfrac{\left(\ddot{d}_{ux} - \ddot{d}_{lx}\right)}{2l} = f_{ux} \cdot l - f_{lx} \cdot l - J_z\Omega\dfrac{\left(\dot{d}_{uy} - \dot{d}_{ly}\right)}{2l} \end{cases} \quad (3)$$

Furthermore, the control forces of radial AMB in four DOFs are

$$
\begin{cases}
f_{ux} = \dfrac{m}{4}\left(\ddot{d}_{ux} + \ddot{d}_{lx}\right) + \dfrac{J_x}{4l^2}\left(\ddot{d}_{ux} - \ddot{d}_{lx}\right) - \dfrac{J_z\Omega}{4l^2}\left(\dot{d}_{uy} - \dot{d}_{ly}\right) \\[2mm]
f_{lx} = \dfrac{m}{4}\left(\ddot{d}_{ux} + \ddot{d}_{lx}\right) - \dfrac{J_x}{4l^2}\left(\ddot{d}_{ux} - \ddot{d}_{lx}\right) + \dfrac{J_z\Omega}{4l^2}\left(\dot{d}_{uy} - \dot{d}_{ly}\right) \\[2mm]
f_{uy} = \dfrac{m}{4}\left(\ddot{d}_{uy} + \ddot{d}_{ly}\right) + \dfrac{J_y}{4l^2}\left(\ddot{d}_{uy} - \ddot{d}_{ly}\right) + \dfrac{J_z\Omega}{4l^2}\left(\dot{d}_{ux} - \dot{d}_{lx}\right) \\[2mm]
f_{ly} = \dfrac{m}{4}\left(\ddot{d}_{uy} + \ddot{d}_{ly}\right) - \dfrac{J_y}{4l^2}\left(\ddot{d}_{uy} - \ddot{d}_{ly}\right) - \dfrac{J_z\Omega}{4l^2}\left(\dot{d}_{ux} - \dot{d}_{lx}\right)
\end{cases}
\tag{4}
$$
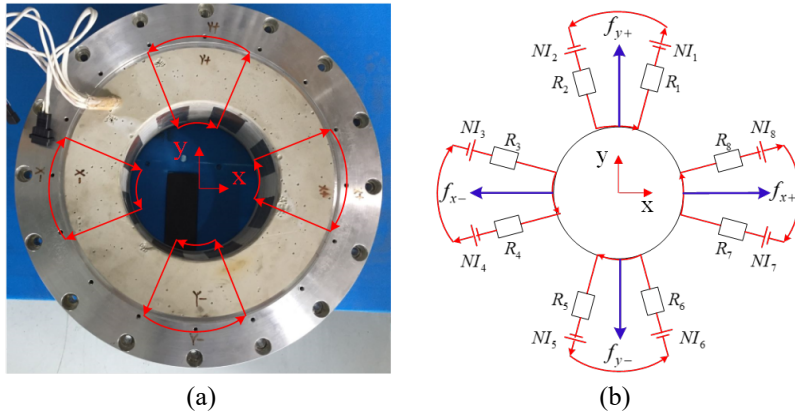
2.2. Modeling of AMB System

Fig. 2. (a) prototype of radial AMB, (b) equivalent magnet circuit of radial AMB.

The prototype of a radial AMB is illustrated in Fig. 2(a), and the equivalent magnet circuit is plotted in Fig. 2(b). The magnet fluxes pass through stator, magnet ring, airgap and rotor. The equivalent reluctances ($R_1 \sim R_8$) of airgap and magnet ring are in series connection within the same magnet pole. N is the turn of winding, and ($I_1 \sim I_8$) are the control currents of winding. The equivalent reluctances of radial AMB in four channels are, respectively

$$
\begin{cases}
R_{y+} = R_1 + R_2 = \dfrac{2d_{y+}}{\mu_0 A_{y+}}; \quad R_{y-} = R_5 + R_6 = \dfrac{2d_{y-}}{\mu_0 A_{y-}} \\[3mm]
R_{x+} = R_7 + R_8 = \dfrac{2d_{x+}}{\mu_0 A_{x+}}; \quad R_{x-} = R_3 + R_4 = \dfrac{2d_{x-}}{\mu_0 A_{x-}}
\end{cases}
\tag{5}
$$

where $d_{n=x+,x-,y+,y-}$ is the radial airgap. μ_0 is the vacuum permeability, and $A_{n=x+,x-,y+,y-}$ is the radial cross-sectional area of magnet pole. The magnet fluxes of radial AMB in four channels are

$$\begin{cases} \Phi_{y+} = \dfrac{NI_1 + NI_2}{R_1 + R_2}; & \Phi_{y-} = \dfrac{NI_5 + NI_6}{R_5 + R_6} \\ \Phi_{x+} = \dfrac{NI_7 + NI_8}{R_7 + R_8}; & \Phi_{x-} = \dfrac{NI_3 + NI_4}{R_3 + R_4} \end{cases} \tag{6}$$

The magnetic forces of radial AMB are

$$\begin{cases} f_{y+} = \dfrac{\Phi_{y+}^2}{\mu_0 A_{y+}}; & f_{y-} = \dfrac{\Phi_{y-}^2}{\mu_0 A_{y-}} \\ f_{x+} = \dfrac{\Phi_{x+}^2}{\mu_0 A_{x+}}; & f_{x-} = \dfrac{\Phi_{x-}^2}{\mu_0 A_{x-}} \end{cases} \tag{7}$$

The resultant magnetic forces of radial AMB are

$$\begin{cases} f_x = f_{x+} - f_{x-} = \dfrac{\mu_0 A N^2}{4} \left[\dfrac{(I_0 + i_x)^2}{(d_0 - d_x)^2} - \dfrac{(I_0 - i_x)^2}{(d_0 + d_x)^2} \right] \\ f_y = f_{y+} - f_{y-} = \dfrac{\mu_0 A N^2}{4} \left[\dfrac{(I_0 + i_y)^2}{(d_0 - d_y)^2} - \dfrac{(I_0 - i_y)^2}{(d_0 + d_y)^2} \right] \end{cases} \tag{8}$$

where I_0 is the bias current, and i_x and i_y are control currents. The derivative of magnetic force with respect to displacement is the displacement stiffness, and the derivative of magnetic force with respect to current is the current stiffness. The current stiffness k_{ix} and the displacement stiffness k_{dx} are

$$\begin{cases} k_{ix} = k_{iy} = \dfrac{\mu_0 A N^2 I_0}{d_0^2} \\ k_{dx} = k_{iy} = \dfrac{\mu_0 A N^2 I_0^2}{d_0^3} \end{cases} \tag{9}$$

The magnetic forces of AMB system are

$$\begin{cases} f_{ux} = k_{ix} i_{ux} - k_{dx} d_{ux}; & f_{lx} = k_{ix} i_{lx} - k_{dx} d_{lx} \\ f_{uy} = k_{iy} i_{uy} - k_{dy} d_{uy}; & f_{ly} = k_{iy} i_{ly} - k_{dy} d_{ly} \end{cases} \tag{10}$$

Therefore, the equivalent model of magnetic force is used to design the control model of MSM rotor.

2.3. Deviation Characteristics of MSM Rotor

When the biased displacement d_0 and the cross-sectional area A of the AMB deflects from the nominal values at the initial installation, the relationships among the current stiffness,

the displacement stiffness and the biased displacement are shown in Fig. 3. In radial direction, the biased displacement is defined as 1mm, and the deviation range is 0.2mm. The nominal value of the radial current stiffness is 620N/A, and the nominal displacement stiffness is -2800N/mm in radial direction. When the biased displacement deflects 0.1mm from the biased value, the deflection value of the radial current stiffness is 100N/A as marked by the red line in Fig. 3(a), and the deflection of the radial displacement stiffness is 1000N/mm in Fig. 3(b). When the axial biased displacement sets at 1.3mm with 0.2mm deviation range, the nominal value of the axial current stiffness is 470N/A, and the nominal displacement stiffness is -1700N/mm in axial direction. If the axial displacement of MSM rotor deflects 0.1mm from the equilibrium position, the deviation term of axial current stiffness is 60N/A, and the deflection value of axial displacement stiffness is 350N/mm.
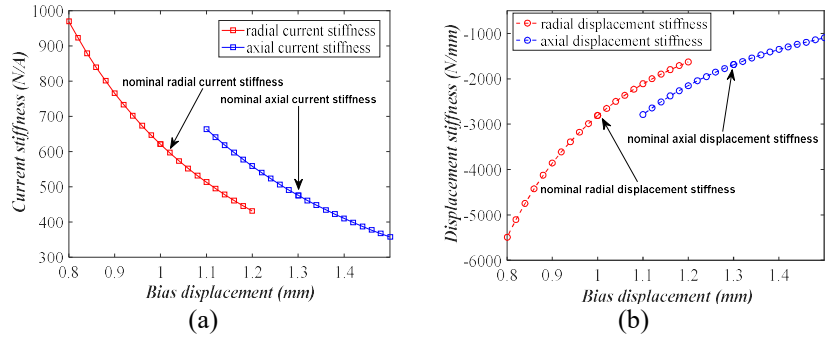

Fig. 3. (a) Current stiffness versus biased displacement, (b) displacement stiffness versus biased displacement.
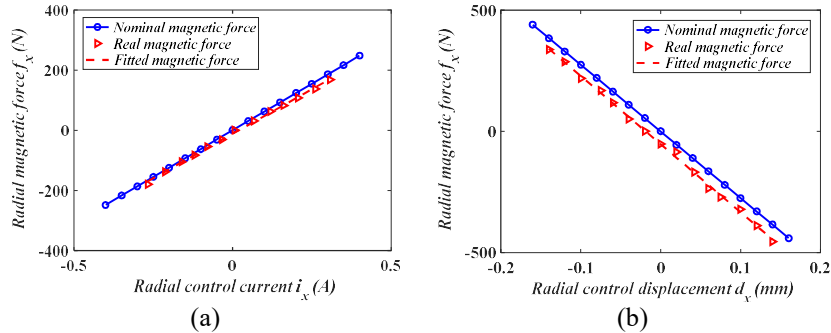

Fig. 4. (a) Radial magnetic force versus control current, (b) radial magnetic force versus displacement.

Moreover, the comparison between the calculated and measured results is shown in Fig. 4, the nominal value is marked by the blue line, and the measured result is marked by the red line. As shown in Fig. 4(b), the measured result of the radial current stiffness is 608N/A, and the measured result of radial displacement stiffness is -2810N/mm. As illuminated in Fig. 5, the measured result of the axial current stiffness is 480N/A, and the measured value of the axial displacement stiffness is -1702N/mm. Therefore, there are differences between the nominal

results and the measured results, so the deviation of the AMB could affect the stability of MSM rotor.
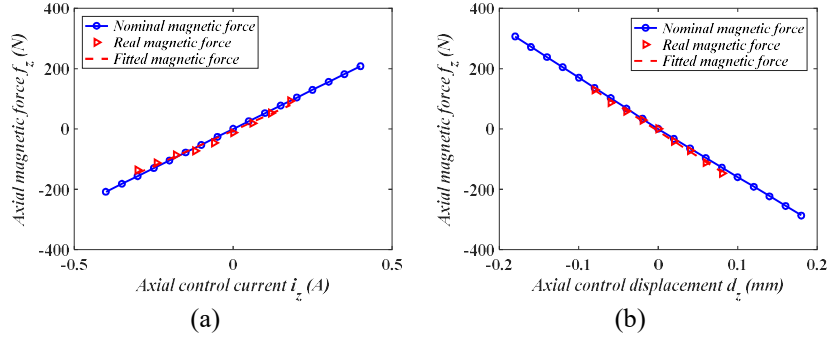

Fig. 5. (a) Axial magnetic force versus control current, (b) axial magnetic force versus displacement.

2.4. Control Model of MSM Rotor

Substituting (10) into (4), the control currents of radial AMB in four channels are

$$
\begin{cases}
i_{ux} = a_0\ddot{d}_{ux} + a_1 d_{ux} + a_2\ddot{d}_{lx} - a_3\left(\dot{d}_{uy} - \dot{d}_{ly}\right) \\
i_{lx} = a_0\ddot{d}_{lx} + a_1 d_{lx} + a_2\ddot{d}_{ux} + a_3\left(\dot{d}_{uy} - \dot{d}_{ly}\right) \\
i_{uy} = a_0\ddot{d}_{uy} + a_1 d_{uy} + a_2\ddot{d}_{ly} + a_3\left(\dot{d}_{ux} - \dot{d}_{lx}\right) \\
i_{ly} = a_0\ddot{d}_{ly} + a_1 d_{ly} + a_2\ddot{d}_{uy} - a_3\left(\dot{d}_{ux} - \dot{d}_{lx}\right)
\end{cases}
\tag{11}
$$

where $a_0 = \dfrac{ml^2 + J_x}{4k_{ix}l^2}$, $a_1 = \dfrac{k_{dx}}{k_{ix}}$, $a_2 = \dfrac{ml^2 - J_x}{4k_{ix}l^2}$ and $a_3 = \dfrac{J_z\Omega}{4k_{ix}l^2}$.

Obviously, there are coupling terms in four control channels of MSM rotor in (11). For example, as shown the first function in (11), in the upper end of x-axis control channel, besides the displacement control term d_{ux}, there are displacement terms d_{lx}, d_{uy} and d_{ly} from other control channels. Therefore, a decoupling method should be used to realize decoupling control of MSM rotor in four control channels. For the radial rotation of MSM rotor, the gyroscopic effect related to the rotational speed introduces an additional coupling term. Based on (11), displacements of MSM rotor through the Laplace transform are

$$
\begin{bmatrix}
d_{ux}(s) \\
d_{lx}(s) \\
d_{uy}(s) \\
d_{lx}(s)
\end{bmatrix}
= G_p(s) \cdot
\begin{bmatrix}
i_{ux}(s) \\
i_{lx}(s) \\
i_{uy}(s) \\
i_{lx}(s)
\end{bmatrix}
\tag{12}
$$

where $G_p^{-1}(s) = \begin{bmatrix} A(s) & B(s) \\ -B(s) & A(s) \end{bmatrix}$, $A(s) = \begin{bmatrix} a_0s^2 + a_1 & a_2s^2 \\ a_2s^2 & a_0s^2 + a_1 \end{bmatrix}$ and $B(s) = \begin{bmatrix} -a_3s & a_3s \\ a_3s & -a_3s \end{bmatrix}$.

To realize decoupling control of MSM rotor, the following definition is introduced

$$G_p^{-1}(s) = D(s) + W(s) \tag{13}$$

where $D(s) = \begin{bmatrix} A(s) & 0 \\ 0 & A(s) \end{bmatrix}$ and $W(s) = \begin{bmatrix} 0 & B(s) \\ -B(s) & 0 \end{bmatrix}$. $D(s)$ is the decoupled control matrix, and $W(s)$ is the decoupling matrix.

3. IMC and DIMC Models of MSM Rotor

3.1. IMC Model of MSM Rotor

For the displacement control of MSM rotor in four DOFs, the block diagram of IMC model is illustrated in Fig. 6(a). $r(s)$ is reference input. $d(s)$ is disturbance input. $y(s)$ is output displacement. $G_{IMC}(s)$ is IMC model, and $G_p(s)$ is control plant of MSM rotor. The internal model of MSM rotor is

$$G_m(s) = G_{m+}(s) \cdot G_{m-}(s) \tag{14}$$

where $G_{m+}(s)$ is the irreversible model including pure time-delay and zeros on right half plane, and $G_{m-}(s)$ is the reversible model.

To tune the robust stability of IMC model, the low pass filter $G_f(s)$ with diagonal elements (I is the unit matrix) is chosen as

$$G_f(s) = \frac{1}{(\lambda s + 1)^2} I \tag{15}$$

Furthermore, the IMC model is

$$G_{IMC}(s) = G_{m-}^{-1}(s) \cdot G_f(s) \tag{16}$$

Moreover, based on the IMC model in Fig. 6(b), the equivalent function of IMC model is

$$K(s) = \frac{G_{IMC}(s)}{1 - G_{IMC}(s)G_m(s)} \tag{17}$$

Therefore, the positive integer of low pass filter would make $G_{IMC}(s)$ becomes proper, and the closed-loop system of MSM rotor could be arbitrarily robust by regulating λ.
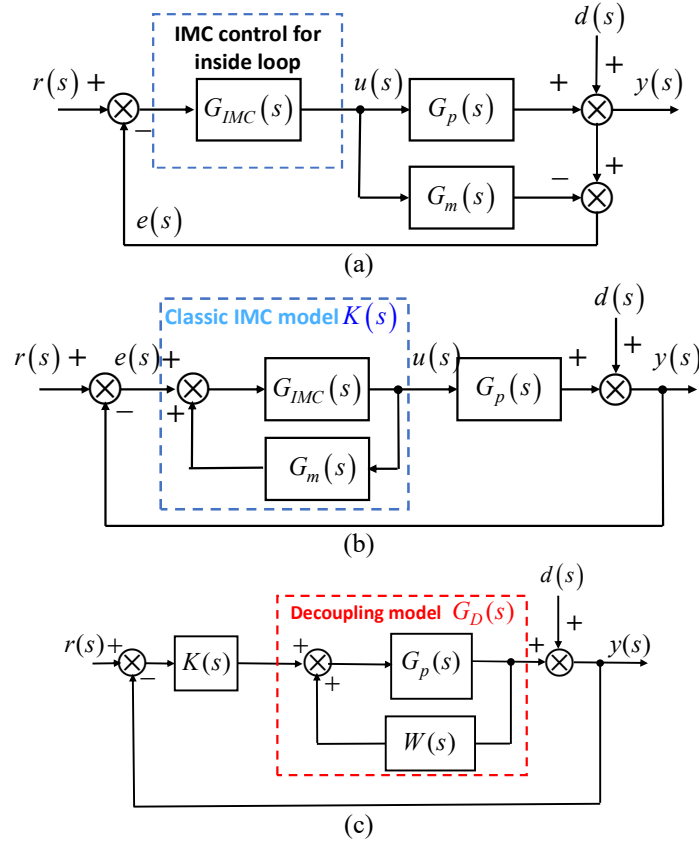
Fig. 6. Block diagrams of control models, (a) IMC model, (b) equivalent IMC model, (c) DIMC model.

3.2. DIMC Model of MSM Rotor

To suppress coupling terms in (11), a matrix $W(s)$ in (13) is introduced to realize the decoupling control of MSM rotor, and then the control plant is decoupled by using a feedback loop illustrated in Fig. 6(c). $K(s)$ is the control model. The model transfer function is

$$G_D(s) = \frac{G_p(s)}{1 - G_p(s)W(s)} \tag{18}$$

Using the decoupling matrix $W(s)$ in (13), the decoupling model yields

$$G_D(s) = D^{-1}(s) \tag{19}$$

Therefore, the DIMC model could be achieved as following

$$G_{DIMC}(s) = G_D(s)D(s) = \frac{G_p(s)}{1 - G_p(s)W(s)} D(s) \tag{20}$$

For an originally decoupled system, this decoupling model is not necessary, so the feedback loop would be omitted, and the standard IMC model of control plant could be applied. Moreover, based on (14), the IMC could be designed for reversible model of MSM

rotor, so the stability of IMC model and control plant could be easily testified.

3.3. Tracking Performance and Sensitivity Analysis

For the IMC model of MSM rotor in Fig. 6(b), the transfer function between reference input $r(s)$ and output displacement $y(s)$ is

$$G_{ry}(s) = \frac{y(s)}{r(s)} = \frac{K(s)G_p(s)}{1 + K(s)G_p(s)} \tag{21}$$

The error between reference input $r(s)$ and output displacement $y(s)$ is

$$e(s) = r(s) - y(s) = \frac{1}{1 + K(s)G_p(s)} r(s) \tag{22}$$

If the control plant is exact to the real plant, there is

$$|e(s)| = \left| \frac{1}{1 + K(s)G_p(s)} r(s) \right|_{G_p = G_m} = 0 \tag{23}$$

When error approaches to zero, the IMC model could exactly track the reference input. If there is a deviation Δa_i of the ith plant parameter a_i from the nominal value, the tracking performance with uncertain parameter is

$$\frac{G_{ry}^{-1}(s)\Delta G_{ry}(s)}{a_i^{-1}\Delta a_i} \to a_i G_{ry}^{-1}(s)\frac{\partial G_{ry}(s)}{\partial a_i} \quad \text{as } \Delta a_i \to 0 \tag{24}$$

The sensitivity function of IMC model is

$$S(s) = a_i G_{IMC}^{-1}(s)\frac{\partial G_{IMC}(s)}{\partial a_i}\bigg|_{G_p(s)=G_m(s)} \tag{25}$$

For the IMC model, substituting the IMC model $G_{IMC}(s)$ in (16) into (25), the sensitivity function of IMC model is

$$S_{IMC}(s) = a_i\left[G_{m-}^{-1}(s)G_f(s)\right]^{-1}\frac{\partial\left[G_{m-}^{-1}(s)G_f(s)\right]}{\partial a_i}\bigg|_{G_p(s)=G_m(s)} = a_i G_{m-}(s)\frac{\partial G_{m-}^{-1}(s)}{\partial a_i} \tag{26}$$

For the DIMC model, substituting the DIMC model $G_{DIMC}(s)$ in (20) into (25), the sensitivity function of DIMC model is

$$S_{DIMC}(s) = a_i\left[\frac{\partial G_D(s)}{\partial a_i}D(s) + G_D(s)\frac{\partial D(s)}{\partial a_i}\right]\bigg|_{G_p(s)=G_m(s)} \tag{27}$$

If $G_p(s)$ is the exact model, so

$$\frac{\partial G_p(s)}{\partial a_i} = 0 \tag{28}$$

Differentiating (18) with respect to a_i, we have

$$\frac{\partial G_D(s)}{\partial a_i} = G_D(s)\frac{\partial W(s)}{\partial a_i}G_D(s)\bigg|_{G_p(s)=G_m(s)} = D^{-1}(s)\frac{\partial W(s)}{\partial a_i}D^{-1}(s) \tag{29}$$

Furthermore, the sensitivity function is

$$S_{DIMC}(s) = a_i D^{-1}(s)\left[\frac{\partial W(s)}{\partial a_i}D^{-1}(s)D(s) + \frac{\partial D(s)}{\partial a_i}\right] = a_i D^{-1}(s)\frac{\partial G_m^{-1}(s)}{\partial a_i} \tag{30}$$

Finally, the sensitivity functions of IMC and DIMC models are

$$\begin{cases} S_{IMC}(s) = a_i G_{m-}(s)\dfrac{\partial G_{m-}^{-1}(s)}{\partial a_i} \\[3mm] S_{DIMC}(s) = a_i D^{-1}(s)\dfrac{\partial G_m^{-1}(s)}{\partial a_i} \end{cases} \tag{31}$$

3.4. Disturbance Rejection and Robustness

For the IMC model in Fig. 6(b), the disturbance transfer function between disturbance input $d(s)$ and output displacement $y(s)$ is

$$G_{dy}^{IMC}(s) = \frac{y(s)}{d(s)} = \frac{1}{1+K(s)G_p(s)} = \frac{1-G_{m-}^{-1}(s)G_f(s)G_m(s)}{1+G_{m-}^{-1}(s)G_f(s)\left[G_p(s)-G_m(s)\right]} \tag{32}$$

If the control plant is exact, the response magnitude of disturbance transfer function is

$$\left|G_{dy}^{IMC}(s)\right| = \left|\frac{1}{1+K(s)G_p(s)}\bigg|_{G_p(s)=G_m(s)}\right| = \left|1-G_f(s)\right| \tag{33}$$

So, the robustness is determined by filter parameter. The response magnitude increases with the filter parameter λ, so a small value of λ could improve the robustness. For the high-frequency disturbance, the robustness of IMC model would be decreased, so a low-pass filter is better for IMC model.

Based on Fig. 6(c), the disturbance transfer function of DIMC model is

$$G_{dy}^{DIMC}(s) = \frac{y(s)}{d(s)} = \frac{1}{1+K(s)G_D(s)} \tag{34}$$

For the exact control plant, the response magnitude is

$$\left|G_{dy}^{DIMC}(s)\right| = \left|1 - G_f(s)\right| \tag{35}$$

Comparing (35) to (33), the DIMC model has same performance on the robustness as the IMC model, and the robustness of closed-loop system is determined by filter parameters.

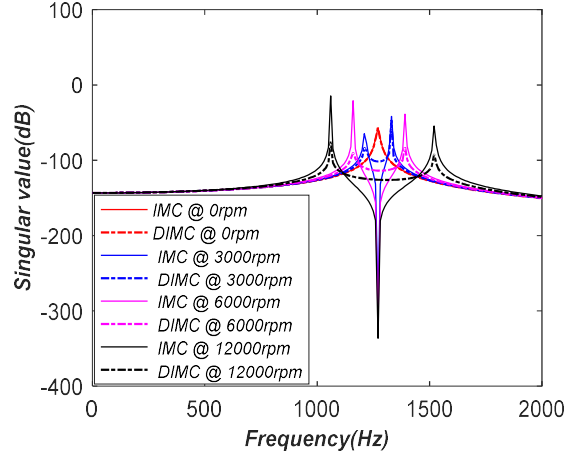## 4. Simulation

4.1. Sensitivity Analysis of MSM Rotor

Fig. 7. Singular values of IMC and DIMC models.

In a multi-input multi-output system, the singular values of frequency function are used to evaluate frequency responses, and the singular values are

$$\sigma_i[G(j\omega)] = \sqrt{\delta_i[G^T(-j\omega)G(j\omega)]} \tag{36}$$

where δ_i is the ith eigenvalue.

The relationship between singular value and rotational speed of MSM rotor is plotted in Fig. 7. For MSM rotor at a high speed, the IMC model has the same sensitivity as the DIMC model in the low-frequency range. When the system frequency equals to the natural rotational speed of MSM rotor, the IMC model has a greater sensitivity peak than the DIMC model, so a whirling oscillation of MSM rotor occurs at a high speed. Therefore, the DIMC model is more effective on suppressing the whirling oscillation of MSM rotor at a high speed.

4.2. Tracking Performance and Robustness of MSM Rotor

To test tracking performances of two control models, a step signal of 0.1mm amplitude is used as the reference input. The response curves of IMC and DIMC models are plotted in Fig. 8(a). As shown by blue line in Fig. 8(a), for the IMC model, the maximum error between

response curve and reference input is 0.03mm. The response curve of DIMC model is shown by red line, and the maximum error is 0.02mm. Moreover, the rising time of IMC model is shorter than DIMC model. In addition, an impulse disturbance is imposed on the MSM rotor when it stably suspends at the equilibrium position, and the displacement deflection of MSM rotor is 0.02mm for both IMC and DIMC model. Therefore, the DIMC model could avoid the excessive overshoot, but the rising time and the setting time will increase. With the same filter coefficients of IMC and DIMC models, the response magnitudes for impulse disturbance are the same.

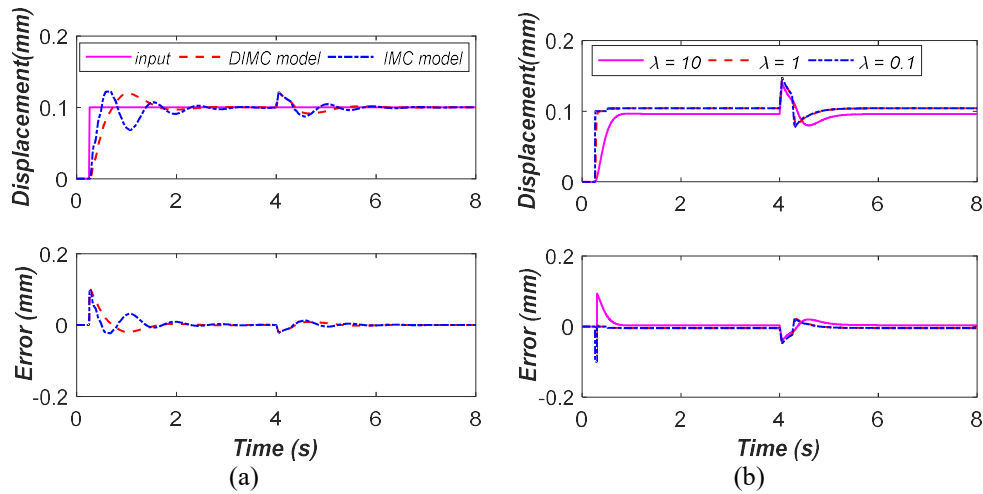(a)   (b)

Fig. 8. (a) Displacement curves of IMC and DIMC model, (b) response curves for impulse disturbance.
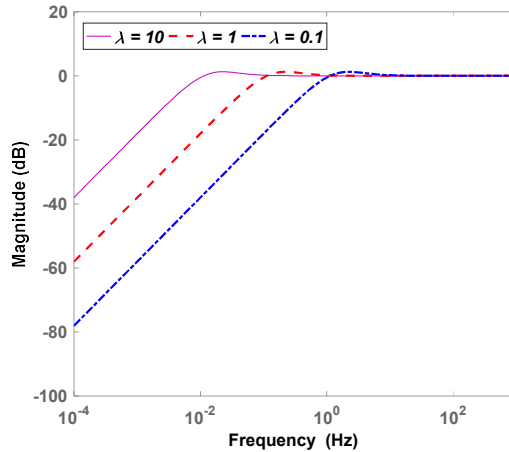

Fig. 9. Response of disturbance transfer function.

In addition, with different values of λ, the response curves of MSM rotor for an impulse disturbance are plotted in Fig. 8(b). The displacement curve is shown by magenta line when λ=10. The error between reference input and response curve is 0.025mm and the settling time is 0.86s. In the meanwhile, the response curve for an impulse disturbance at λ=0.1 is plotted by

blue line. The error is 0.016mm and the settling time is 0.52s. Therefore, the robust stability of MSM rotor is improved with a great value of λ, but the tracking lag is enlarged.

Moreover, response curves of disturbance transfer function in (33) with different values of λ are plotted in Fig. 9. The response magnitude at $\lambda=0.1$ shown by the blue line is greater than that at $\lambda=1$, so the IMC and DIMC models are both sensitive to the disturbance, but the cut-off frequency of disturbance transfer function is decreased with the value of λ. So, the disturbance could affect the robustness of MSM rotor, but a great value of λ could reduce the frequency range of disturbance.

The simulation results indicate that the DIMC model has better performance on reducing overshoot and oscillation but increases the rising time and the setting time.

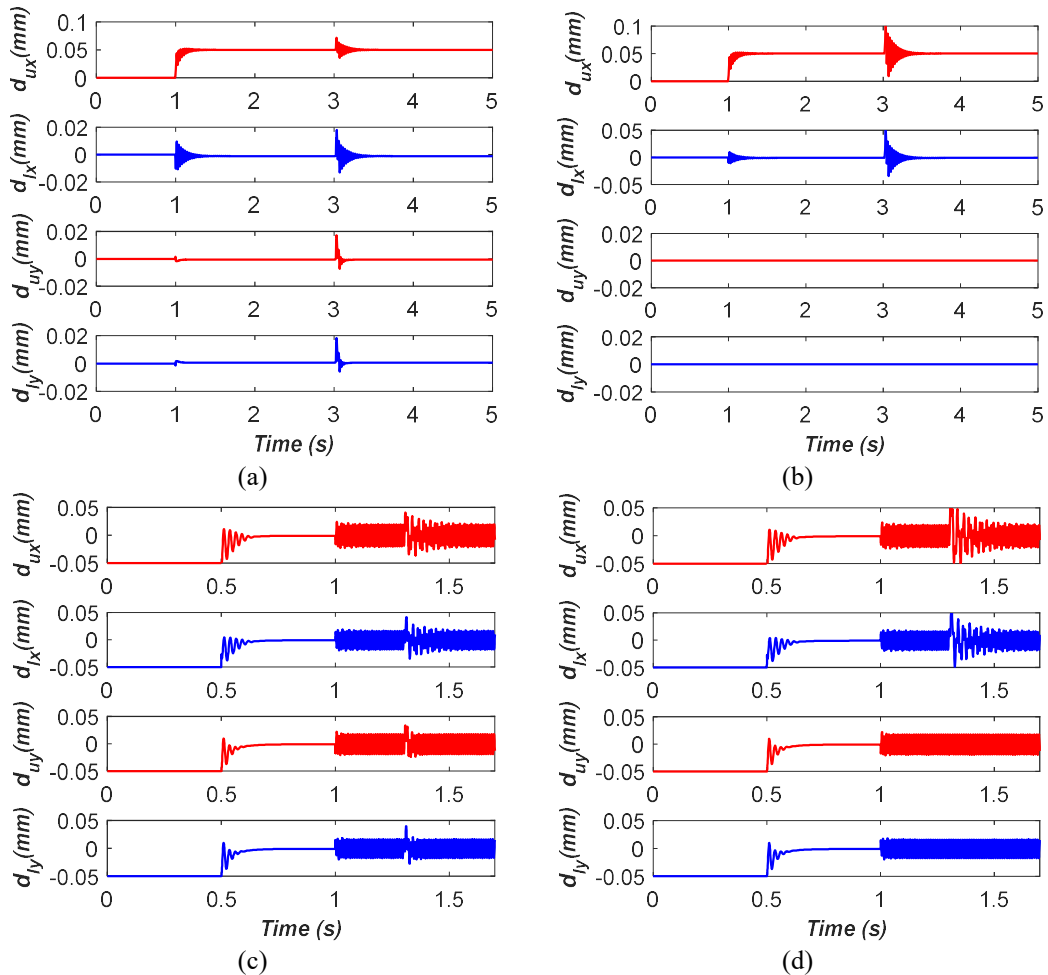## 4.3. Rotation Performance of MSM Rotor with IMC and DIMC Model

Fig. 10. (a) Suspension process of MSM rotor with IMC model, (b) suspension process of MSM rotor with DIMC model, (c) dynamic displacements of MSM rotor with IMC model at 6000rpm, (b) dynamic displacements of MSM rotor with DIMC model at 6000rpm.

The suspension process of MSM rotor with IMC model is plotted in Fig. 10(a). The magnetic force of upper radial AMB at suspends the MSM rotor at the equilibrium position at t=1s. At that instant, there are deflections on other three displacement terms. An impulse disturbance acts on the upper end of MSM rotor when t=3s, the displacement d_{ux} has 0.07mm deflection from the equilibrium position, and a deflection 0.02mm occurs on other three displacement control channels. For the DIMC model, the suspension process of MSM rotor is plotted in Fig. 10(b). When an impulse disturbance is imposed on upper end of MSM rotor at t=3s, the displacement d_{ux} has 0.08mm deflection, and the displacement d_{lx} has a deflection about 0.03mm, but displacements d_{uy} and d_{ly} still maintain at the balanced state.

Furthermore, dynamic displacements of MSM rotor with IMC model at 6000rpm are plotted in Fig. 10(c). The stable displacement amplitude of MSM rotor is 0.015mm. When an impulse disturbance is imposed on the upper end of x-axis, deflections of d_{ux} and d_{lx} are both 0.05mm, and deflections of d_{uy} and d_{ly} are both 0.04mm. The dynamic displacements of MSM rotor with the DIMC model are plotted in Fig. 10(d) The displacement d_{uy} and d_{ly} remain stable, but deflections of d_{ux} and d_{lx} both are 0.06mm.

Therefore, the DIMC model reduces the coupling effect when the MSM rotor works at both static suspension and dynamic rotation states, and deflections of MSM rotor in other displacement channels are avoidable by applying the DIMC model.

5. Experiment

5.1. Experimental Setup

The experiment setup is illustrated in Fig. 11. It consists of a mechanical system and a signal processing system. The mechanical system has two pairs of radial AMBs, one pair of axial AMBs, a FW rotor and a PMSM. The power supply system with 28V and 2A is used to drive axial and radial AMBs. The vacuum pump reduces the wind drag when the MSM rotor works at a high speed. For the signal processing system, the eddy current displacement sensors measure displacement deflections of MSM rotor. The data acquisition (DAQ) board collects and feds back displacement deflections to the main control unit (MCU) based on a digital signal processor (DSP) chip and a field programmable gate array (FPGA) chip. The industrial personal computer (IPC) timely monitors working statuses of experimental setup such as rotational speed and dynamic displacements. The major parameters are listed in TABLE. I.
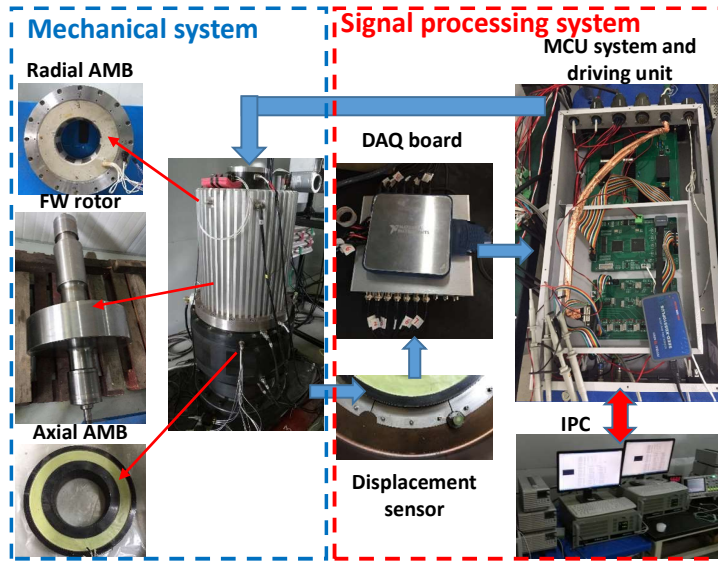
Fig. 11. The experimental setup of MSM rotor.

TABLE. I. PARAMETERS OF EXPERIMENTAL SETUP.

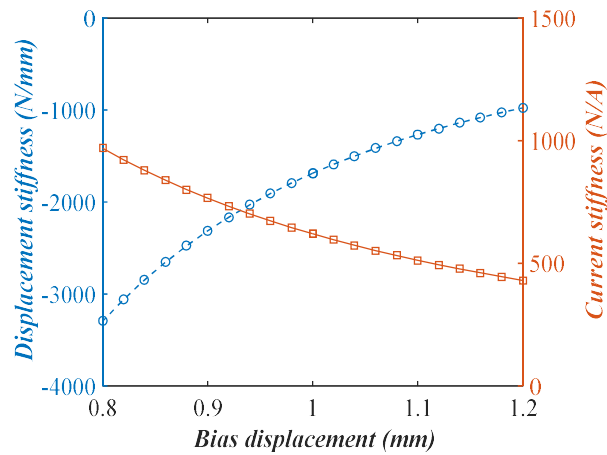| Parameter	Value	Parameter	Value
m	150kg	k_{ix}	620N·A^{-1}
J_x	1.24kg·m^2	k_{dx}	-1700N·mm^{-1}
J_y	1.24kg·m^2	l	0.48mm
J_z	0.67kg·m^2	k_a	0.2A·V^{-1}
λ	0.001	Ω_1	6000rpm
k_s	3.3V/mm	Ω_2	10000rpm

5.2. Sensitive Analysis of MSM Rotor

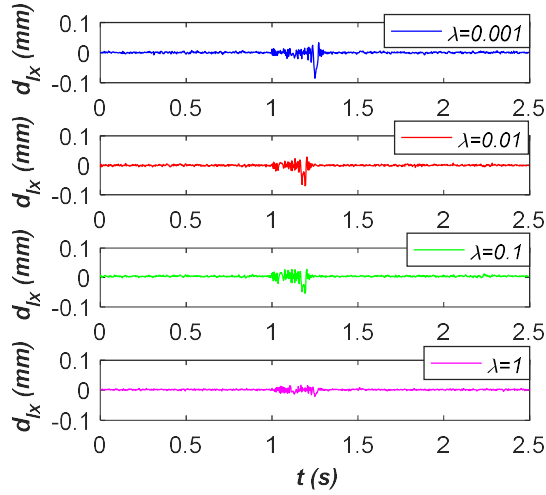Fig. 12. The sensitivity of displacement stiffness and current stiffness.

Fig. 13. Dynamic displacements of MSM rotor with different values of λ.

According to (9), relationships among current stiffness, displacement stiffness and bias displacement are illustrated in Fig. 12. The nominal bias displacement is 1mm, the nominal value of radial current stiffness shown by red line is 620N/A and the nominal value of radial displacement stiffness marked by blue line is -1700N/mm. When the bias displacement deflects 0.1mm from the nominal position, the deflection value of radial current stiffness is 90N/A, and deflection of radial displacement stiffness is 360N/mm. Therefore, for the MSM rotor with great self-weight, the displacement stiffness and the current stiffness are sensitive to the initial position affected by the self-weight.

Moreover, an impulse disturbance (10% of self-weight) is imposed on the lower end of MSM rotor at the equilibrium state. Fig. 13 shows the displacement deflections of MSM rotor with different values of λ. At $\lambda=1$, the response magnitude for impulse disturbance is 0.02mm as shown by blue line. The response magnitude declines to 0.085mm when λ decreases to 0.001. So, the disturbance sensitivity is suppressed by increasing the value of λ.

5.3. Suspension Performance and Anti-Disturbance

Firstly, a step signal is chosen as the reference input to realize MSM rotor's suspension at the equilibrium position, and then an impulse disturbance is added on the lower end of MSM rotor. The suspension traces of MSM rotor with IMC model are shown in Fig. 14(a). The MSM rotor is forced to suspend at the equilibrium position in x-axis at t=5s, so displacements d_{ux} and d_{lx} both equal to zero. At the same instant, displacements d_{uy} and d_{ly} have a deflection 0.07mm because of the coupling effect among four displacement channels. An impulse disturbance is imposed on the lower end of x-axis (displacement d_{lx}) at t=5.5s, it has a

response magnitude 0.08mm. The response magnitude of d_{ux} is 0.04mm. Owing to the coupling effect, displacements d_{ly} and d_{uy} have respective deflection magnitudes of 0.07mm and 0.03mm. Moreover, the suspension traces of MSM rotor with the DIMC model are shown in Fig. 14(b). The displacement deflections of d_{ly} and d_{uy} are both 0.06mm when the MSM rotor is forced to suspend at the equilibrium position in *x*-axis at *t*=4s. The response magnitude of d_{lx} due to the impulse disturbance is 0.07mm while the displacement deflection of d_{ly} is 0.05mm. So, as listed in TABLE. II, the DIMC model has a 28.6% reduction in d_{ly} and 33.3% reduction in d_{uy} compared to the IMC model.
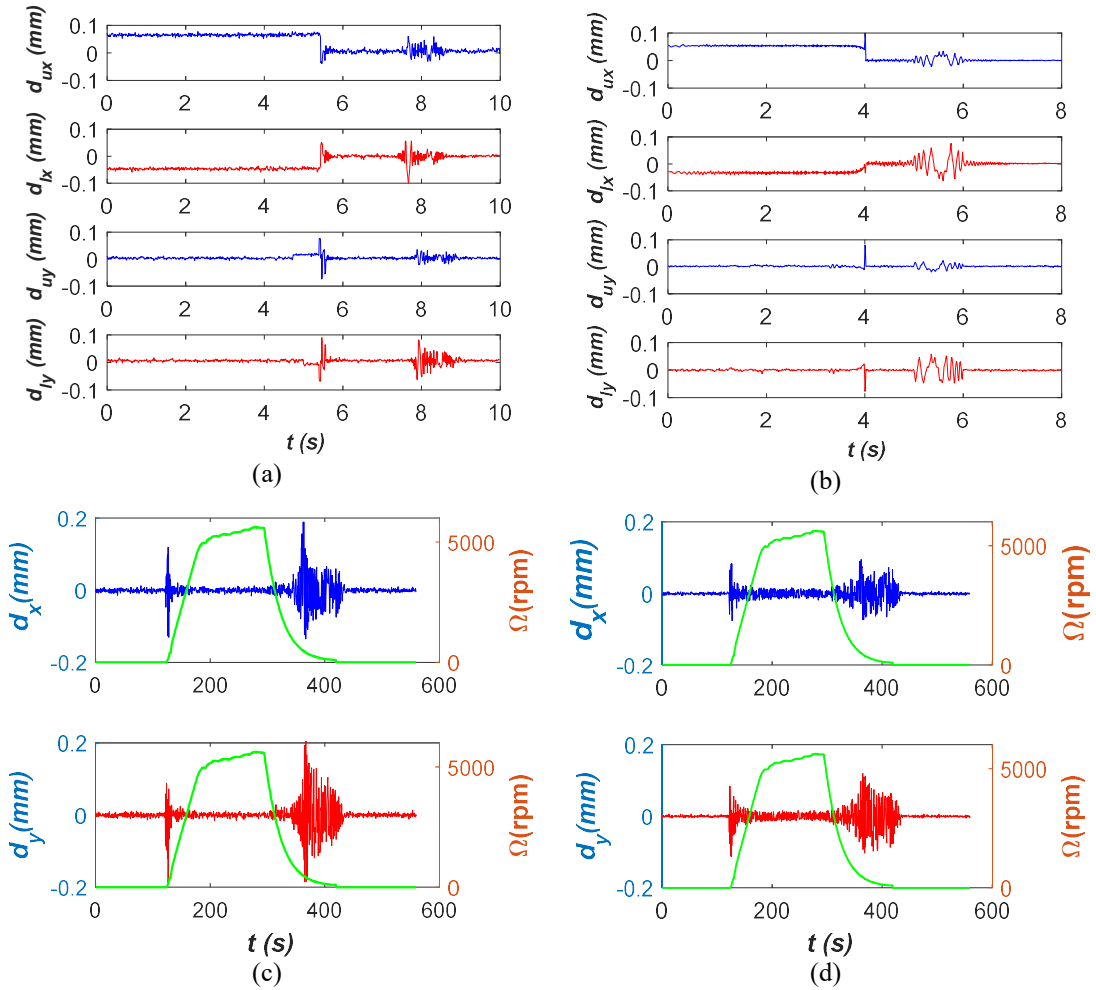

Fig. 14. (a) Suspension traces of MSM rotor with IMC model, (b) suspension traces of MSM rotor with DIMC model, (c) dynamic displacement of MSM rotor with IMC model during speed regulation, (b) dynamic displacement of MSM rotor with DIMC model during speed regulation.

The dynamic displacements of IMC and DIMC models during speed regulation are plotted. The speed curve is plotted by green line when the MSM rotor is accelerated from zero to 5000rpm at *t*=118s and deaccelerated to 0rpm at *t*=418s. The displacements of MSM rotor have deflections at the start moment of acceleration and deceleration. The maximum

displacement deflection of IMC model is 0.15mm during acceleration and that during deceleration is 0.18mm in   Fig. 14(c). Moreover, the DIMC model has maximum displacement deflection 0.08mm during acceleration and that during deceleration is 0.09mm in Fig. 14(d). Therefore, the DIMC model has a reduction of displacement deflection 50% in comparison with the IMC model.

The dynamic displacements of MSM rotor with the IMC model are plotted in Fig. 15(a) when the speed is 6000rpm. The stable displacement of MSM rotor is 0.025mm. When an impulse disturbance is imposed on lower end of x-axis, the response magnitude of d_{lx} is 0.08mm, and that of d_{ux} is 0.03mm. Along y-axis, the response amplitude of d_{ly} is 0.04mm, and that of d_{uy} is 0.03mm. Fig. 15(b) displays dynamic displacements of MSM rotor with using the DIMC model. The stable displacement of MSM rotor is 0.015mm. The deflection of d_{lx} is 0.05mm, and that of d_{ux} is 0.03mm. At the same instant, the response amplitude of d_{ly} for impulse disturbance is 0.035mm. Consequently, based on the comparison in TABLE. III, the DIMC model has 12.5% reduction in deflection of d_{ly} and 16.7% reduction in deflection of d_{uy} compared with the IMC model.

The dynamic displacements of IMC model are shown in Fig. 15(c) when the speed of MSM rotor is 10000rpm. The stable amplitude of MSM rotor is 0.015mm. When an impulse disturbance is imposed on the lower end of MSM rotor in x-axis, the deflection of d_{lx} for impulse disturbance is 0.09mm, and that of d_{ux} is 0.03mm. For the disturbance response in y-axis, the deflection of d_{ly} is 0.08mm, and that of d_{uy} is 0.03mm. The dynamic displacements of MSM rotor with applying DIMC model are shown in Fig. 15(d). The stable suspension displacement of MSM rotor is 0.01mm. When the disturbance is applied on lower end of x-axis, the response amplitude of d_{lx} for impulse disturbance is 0.07mm, and that of d_{ux} is 0.03mm. The response amplitude of d_{ly} for impulse disturbance is 0.07mm, and that of d_{uy} is 0.02mm. Therefore, the DIMC model has a 12.5% deflection reduction in d_{ly} and 33.3% reduction in d_{uy} in comparison with the IMC model.
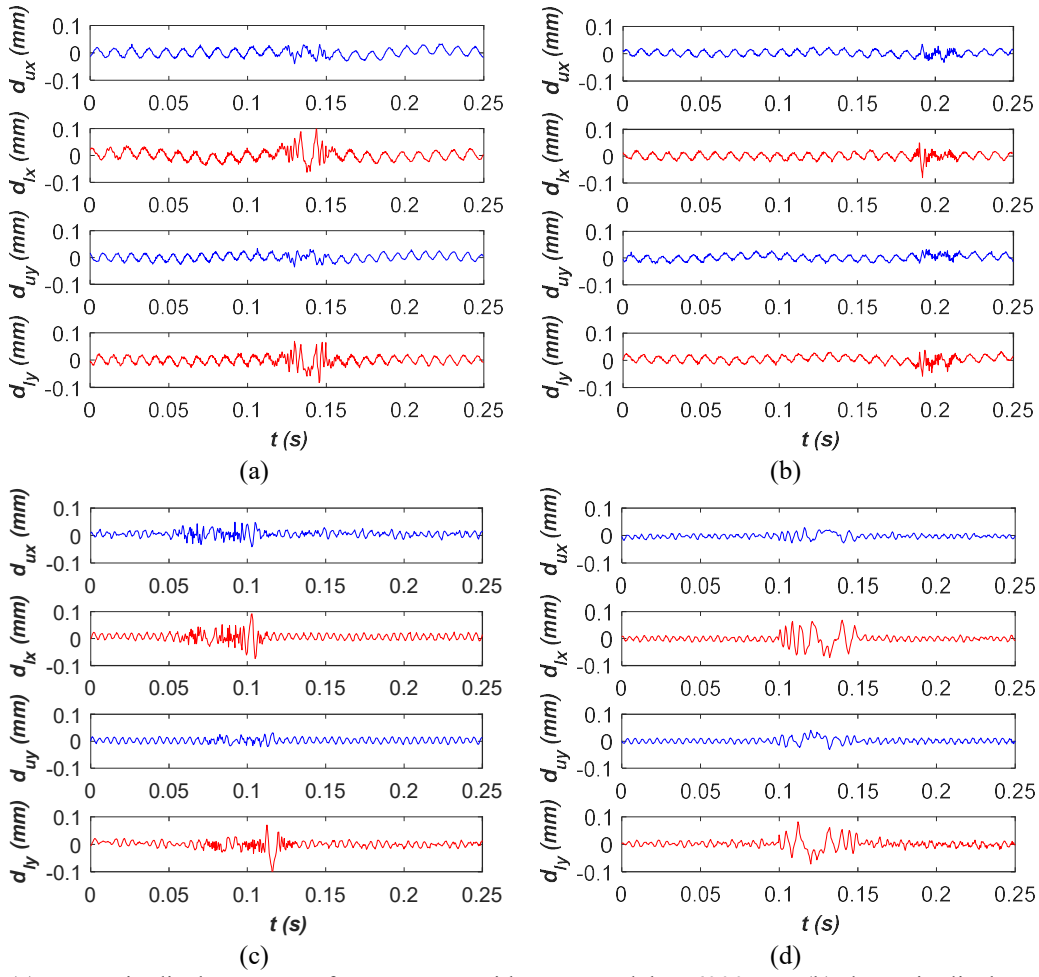
Fig. 15. (a) Dynamic displacements of MSM rotor with IMC model at 6000rpm, (b) dynamic displacements of MSM rotor with DIMC model at 6000rpm, (c) dynamic displacements of MSM rotor with IMC model at 10000rpm, (d) dynamic displacements of MSM rotor with DIMC model at 10000rpm.

TABLE. II. COMPARISON (d_{ly}) o IMC and DIMC MODEL

State of MSM	IMC model	DIMC model	Reduction
Suspension	0.07mm	0.06mm	14.3%
Static disturbance	0.07mm	0.05mm	28.6%
6000rpm	0.04mm	0.035mm	12.5%
10000rpm	0.08mm	0.07mm	12.5%

TABLE. III. COMPARISON (d_{uy}) of IMC and DIMC MODEL

State of MSM	IMC model	DIMC model	Reduction
Suspension	0.07mm	0.06mm	14.3%
Static disturbance	0.03mm	0.02mm	33.3%
6000rpm	0.03mm	0.025mm	16.7%
10000rpm	0.03mm	0.02mm	33.3%

21

6. Conclusion

In static suspension state, the robustness of MSM rotor is improved by tuning the parameters of IMC model. Moreover, the DIMC model is applied to realize decoupling control in four DOFs, and displacement deflections of MSM rotor caused by the coupling effect are mitigated. In dynamical rotation state, dynamic displacements of MSM rotor are mitigated by both IMC and DIMC models. Although the displacement overshoot of MSM rotor with the IMC model still exists, the IMC model could improve the robustness of MSM rotor, and the DIMC model suppresses the coupling effect among different control channels.

Funding Acknowledgement

Conflict of Interest Statement

The authors declare no conflict of interest in preparing this article.

References

Ahrens M, Kucera L and Larsonneur R. (1996) Performance of a magnetically suspended flywheel energy storage device. *IEEE Transactions on Control Systems Technology* 4(5): 494-502.

Asama J, Kanehara D, Oiwa T, et al. (2014) Development of a compact centrifugal pump with a two-axis actively positioned consequent-pole bearingless motor. *IEEE Transactions on Industry Applications* 50(1): 288-295.

Barbaraci G. (2016) Axial active magnetic bearing design. *Journal of Vibration and Control* 22(5): 1190-1197.

Barbaraci G, Mariotti GV and Piscopo A. (2013) Active magnetic bearing design study. *Journal of Vibration and Control* 19(16): 2491-2505.

Cole MOT and Fakkaew W. (2018) An Active Magnetic Bearing for Thin-Walled Rotors: Vibrational Dynamics and Stabilizing Control. *IEEE/ASME Transactions on Mechatronics* 23(6): 2859-2869.

Couzon P-Y and Der Hagopian J. (2007) Neuro-fuzzy active control of rotor suspended on active magnetic bearing. *Journal of Vibration and Control* 13(4): 365-384.

Cui P and Cui J. (2017) Harmonic current suppression of active-passive magnetically suspended control moment gyro based on variable-step-size FBLMS. *Journal of Vibration and Control* 23(8): 1221-1230.

Fang J and Ren Y. (2010) High-precision control for a single-gimbal magnetically suspended control moment gyro based on inverse system method. *IEEE Transactions on Industrial Electronics* 58(9): 4331-4342.

Garcia CE and Morari M. (1982) Internal model control. A unifying review and some new

results. *Industrial & Engineering Chemistry Process Design and Development* 21(2): 308-323.

Guo Q, Liu G, Xiang B, et al. (2016) Robust control of magnetically suspended gimbals in inertial stabilized platform with wide load range. *Mechatronics* 39: 127-135.

Haiping D, Nong Z, Ji JC, et al. (2010) Robust Fuzzy Control of an Active Magnetic Bearing Subject to Voltage Saturation. *IEEE Transactions on Control Systems Technology* 18(1): 164-169.

Han B, Xu Q and Yuan Q. (2016) Multiobjective optimization of a combined radial-axial magnetic bearing for magnetically suspended compressor. *IEEE Transactions on Industrial Electronics* 63(4): 2284-2293.

Li S and Gu H. (2012) Fuzzy adaptive internal model control schemes for PMSM speed-regulation system. *IEEE Transactions on Industrial Informatics* 8(4): 767-779.

Li Y, Zheng L, Liang Y, et al. (2020) Adaptive compensation control of an electromagnetic active suspension system based on nonlinear characteristics of the linear motor. *Journal of Vibration and Control*: 1077546320909985.

Masuzawa T, Ezoe S, Kato T, et al. (2003) Magnetically suspended centrifugal blood pump with an axially levitated motor. *Artificial organs* 27(7): 631-638.

Noshadi A, Shi J, Lee WS, et al. (2017) Robust control of an active magnetic bearing system using H∞ and disturbance observer-based control. *Journal of Vibration and Control* 23(11): 1857-1870.

Parada M, Sbarbaro D, Borges RA, et al. (2017) Robust PI and PID design for first-and second-order processes with zeros, time-delay and structured uncertainties. *International Journal of Systems Science* 48(1): 95-106.

Pesch AH, Smirnov A, Pyrhonen O, et al. (2015) Magnetic Bearing Spindle Tool Tracking Through -Synthesis Robust Control. *IEEE/ASME Transactions on Mechatronics* 20(3): 1448-1457.

Rivera D, Morarl M and Skogestad S. (1986) Internal Model Control: Pid Controller Design. *Industrial and Engineering Chemistry Process Design and Development* 25(1): 252-265.

Rubio JdJ. (2018) Robust feedback linearization for nonlinear processes control. *ISA transactions* 74: 155-164.

Rubio JdJ, Aguilar A, Meda-Campaña JA, et al. (2019) An Electricity Generator Based on the Interaction of Static and Dynamic Magnets. *IEEE Transactions on Magnetics* 55(8): 1-11.

Sun X, Su B, Chen L, et al. (2017) Precise control of a four degree-of-freedom permanent magnet biased active magnetic bearing system in a magnetically suspended direct-driven spindle using neural network inverse scheme. *Mechanical Systems and Signal Processing* 88: 36-48.

Tang J, Wang K and Xiang B. (2017) Stable Control of High-Speed Rotor Suspended by Superconducting Magnetic Bearings and Active Magnetic Bearings. *IEEE Transactions on Industrial Electronics* 64(4): 3319-3328.

Wang K, Ma X, Liu Q, et al. (2019) Multiphysics Global Design and Experiment of the Electric Machine With a Flexible Rotor Supported by Active Magnetic Bearing. *IEEE/ASME Transactions on Mechatronics* 24(2): 820-831.

Wei C and Söffker D. (2016) Optimization strategy for PID-controller design of AMB rotor systems. *IEEE Transactions on Control Systems Technology* 24(3): 788-803.

Xiang B and on Wong W. (2019) Vibration characteristics analysis of magnetically suspended rotor in flywheel energy storage system. *Journal of Sound and Vibration* 444: 235-247.

Xiang B and Tang J. (2015) Suspension and titling of vernier-gimballing magnetically suspended flywheel with conical magnetic bearing and Lorentz magnetic bearing.

Mechatronics 28: 46-54.

Zad HS, Khan TI and Lazoglu I. (2018) Design and adaptive sliding-mode control of hybrid magnetic bearings. *IEEE Transactions on Industrial Electronics* 65(3): 2537-2547.

Zheng S and Feng R. (2016) Feedforward compensation control of rotor imbalance for high-speed magnetically suspended centrifugal compressors using a novel adaptive notch filter. *Journal of Sound and Vibration* 366: 1-14.